Motion Artifacts of Extended High Frame Rate Imaging

Jing Wang and Jian-yu Lu, *Senior Member, IEEE*

Abstract*—Based on the high frame rate (HFR) imaging method developed in our lab, an extended high frame rate imaging method with various transmission schemes was developed recently. In this method, multiple, limited-diffraction array beams or steered plane wave transmissions are used to increase image resolution and field of view as well as to reduce sidelobes. Furthermore, the multiple, limited-diffraction array beam transmissions can be approximated with square-wave aperture weightings, allowing one or two transmitters to be used with a multielement array transducer to simplify imaging systems. By varying the number of transmissions, the extended HFR imaging method allows a continuous trade-off between image quality and frame rate. Because multiple transmissions are needed to obtain one frame of image for the method, motion could cause phase misalignment and thus produce artifacts, reducing image contrast and resolution and leading to an inaccurate clinical interpretation of images. Therefore, it is important to study how motion affects the method and provide a useful guidance of using the method properly in various applications. In this paper, computer simulations, *in vitro* and *in vivo* experiments were performed to study the effects of motion on the method in different conditions. Results show that a number of factors may affect the motion effects. However, it was found that the extended HFR imaging method is not sensitive to the motions commonly encountered in the clinical applications, as is demonstrated by an *in vivo* heart experiment, unless the number of transmissions is large and objects are moving at a high velocity near the surface of a transducer.

I. Introduction

Stratton [1] studied a single-frequency beam with Bessel transverse profile first and gave the name “undistorted progressive wave”. Later, Durnin [2] and Durnin *et al.* [3] studied the Bessel beam again and gave the term “nondiffracting beam” or “diffraction-free beam”. Because, given finite aperture and energy, practical beams will eventually diffract, the term “limited-diffraction beam” was used in 1993 [4] to represent “nondiffracting beams”. In the early 1990s, new families of limited-diffraction beams were discovered [5]–[7]. These waves were termed X waves because the shape of the waves in a plane through the axial axis of the waves resembles the letter “X” [5]–[9], and they were described in the “Search and Discovery” column of [10]. The advantage of limited-diffraction beams is that, when produced with finite aperture and energy, they do not diffract over a very large depth of field [11], [12]. Because of this property, limited-diffraction beams and other related beams have been studied extensively by many researchers in various fields, such as, medical imaging [13]–[16], tissue characterization [17], nondestructive evaluation (NDE) of industrial materials [18], transverse blood flow velocity estimation [19], high-speed flow velocity vector imaging [20], fast-field computation for two-dimensional (2-D) array transducers [21], optical communications [22], optical coherent tomography [23], and physics [24], [25].

Based on X wave theories [5]–[9], Lu developed a high frame rate (HFR) imaging method in the 1990s [26]–[28] in which a pulsed plane wave was used in transmission and limited-diffraction array beam weightings [29]–[32] were applied to received echo signals to produce a spatial Fourier transform of an object function for a two-dimensional (2-D) or three-dimensional (3-D) image reconstruction. This method was featured in a review paper [33] and was described as “an intriguing development in high-speed imaging” in [34]. Because single transmission is used to produce one image, in principle, an ultra-high frame rate (up to 3750 volumes/s for biological soft tissues at a depth of 200 mm) can be achieved. Combined with computationally efficient fast Fourier transform (FFT) and inverse FFT, simpler imaging system can be constructed. Recently, the HFR imaging method has been extended in our lab to include various transmission schemes such as limited-diffraction array beam [29], [30] and steered plane wave [31], [32] with multiple transmissions, which allow a continuous trade-off between image quality and imaging frame rate [35]–[41]. In addition, square wave, instead of exact sine and cosine, aperture voltage weightings can be used for limited-diffraction array beam transmissions and receptions to improve image penetration given a fixed transmit voltage and thus simplify imaging systems [35]–[37].

Phase coherent summation in either spatial or spatial Fourier domain for multiple transmissions is a key to taking advantage of the extended HFR imaging method [35]–[37]. Theoretically, this can be done only when objects are assumed stationary. If objects are moved between transmissions, the summation will not be phase aligned and artifacts may be produced. Motion artifacts have been important research topics in medical imaging because they degrade signal-to-noise ratio (SNR) and image contrast and resolution, and they may cause inaccurate clinical interpretation of images. In medical imaging, motion arti-

Manuscript received August 16, 2006; accepted February 25, 2007. This work was supported in part by the grant, HL60301, from the National Institutes of Health, Bethesda, MD.

The authors are with the Ultrasound Laboratory, Department of Bioengineering, The University of Toledo, Toledo, OH 43606 (e-mail: jilu@eng.utoledo.edu).

Digital Object Identifier 10.1109/TUFFC.2007.391

facts may be caused by many factors, including physiological phenomena such as breath, blood flow, and cardiac motions. In addition, motions of patient or operator and mechanical vibrations of the environment also may produce motion artifacts [42].

Many research groups have studied motion artifacts for various methods in ultrasonic imaging. Maurice and Bertrand [43] examined speckle-motion artifacts under tissue shearing. Shen and Li [44] studied motion artifacts of tissue harmonic imaging. Kallel *et al.* [45] examined motion artifacts under tissue rotation. Kallel and Ophir [46], and Taylor *et al.* [47] discussed motion artifacts for elastography. Shi *et al.* [48] and Wang *et al.* [49] tried to reduce motion artifacts for thermal strain imaging and for hyperthermia phased arrays, respectively. In addition, many researchers studied motion artifacts in synthetic aperture imaging (SAI) [50]–[57]. Despite these studies, the effects of motion on the extended HFR imaging method with various transmission schemes have not yet been studied. Therefore, it is important to study these effects and understand the nature of motion artifacts on this method, so that the method can be used properly in various medical applications, and methods to reduce motion artifacts can be developed in the future. In this paper, the effects of motion on the extended HFR imaging method are studied with computer simulations, *in vitro* experiments on an ATS539 tissue-mimicking phantom (ATS Laboratories, Inc., Bridgeport, CT), and an *in vivo* experiment on the heart of a healthy volunteer with a homemade, general-purpose HFR imaging system [35], [58], [59].

This paper is organized as follows. In Section II, the key formulas of the extended HFR imaging method [35] with multiple, limited-diffraction array beam or steered plane wave transmissions are introduced. Computer simulations showing the effects of motion on the method are given in Section III. Results of *in vitro* experiments on a tissue-mimicking phantom and an *in vivo* experiment on a human heart are presented in Section IV. A discussion and conclusions are given in Sections V and VI, respectively.

II. Theoretical Preliminaries

The following are key formulas of the extended HFR imaging and are used for the image reconstructions in this study [35]. Under the Born approximation (weak scattering or where multiple scattering can be ignored) [60], [61], a relationship between the temporal Fourier transform of echo signals due to a steered plane wave or limited-diffraction array beam transmission and the spatial Fourier transform of the object function is given by the Fourier transform pair (see (8) and (9) of [35]) shown in (1) (see next page), where:

$$\begin{cases} k'_x = k_{x_R} + k_{x_T} \\ k'_y = k_{y_R} + k_{y_T} \\ k'_z = k_{z_R} + k_{z_T} \\ \quad = \sqrt{k^2 - k_{x_R}^2 - k_{y_R}^2} + \sqrt{k^2 - k_{x_T}^2 - k_{y_T}^2} \geq 0 \end{cases}, \tag{2}$$

and "$*$" represents the convolution with respect to time, $R_{k_{x_R}+k_{x_T},k_{y_R}+k_{y_T}}(t)$ (its Fourier transform in terms of time is $\widetilde{R}_{k'_x,k'_y}(\omega)$) is the echo signals of a transducer weighted with a limited-diffraction array beam [29], [30] (see (7) of [35]):

$$\Phi^R_{\text{Array}}(\vec{r}_0,t) = \frac{1}{2\pi}\int_{-\infty}^{\infty} T(k)H(k)e^{ik_{x_R}x_0+ik_{y_R}y_0+ik_{z_R}z_0}e^{-i\omega t}dk, \tag{3}$$

where $\vec{K}^R = (k_{x_R}, k_{y_R}, k_{z_R})$ is the wave vector of the array beam in reception, $k_{z_R} = \sqrt{k^2 - k_{x_R}^2 - k_{y_R}^2} \geq 0$, $\vec{r}_0 = (x_0, y_0, z_0)$ is a point in space, t is the time, k_{x_R} and k_{y_R} are free parameters, $T(k)$ is the transfer function of the transducer in reception [62], $H(k)$ is the Heaviside step function [63], with $k = \omega/c$, where $\omega = 2\pi f$ is the angular frequency, f is the frequency, and c is the speed of sound in the medium. $f(\vec{r}_0)$ is the object function defined in the volume, V, with its 3-D spatial Fourier transform, $F(k'_x, k'_y, k'_z)$.

$$\Phi^T_{\text{Array}}(\vec{r}_0,t) = \frac{1}{2\pi}\int_{-\infty}^{\infty} A(k)H(k)e^{ik_{x_T}x_0+ik_{y_T}y_0+ik_{z_T}z_0}e^{-i\omega t}dk \tag{4}$$

is a limited-diffraction array beam in transmission (see (6) of [35]) with a transmission wave vector of $\vec{K}^T = (k_{x_T}, k_{y_T}, k_{z_T})$, $k_{z_T} = \sqrt{k^2 - k_{x_T}^2 - k_{y_T}^2} \geq 0$, and $A(k)$ is the transfer function of the transducer in transmission. Because of the relationship between a limited-diffraction array beam aperture weighting and a 2-D Fourier transform of echo signals over the same transducer aperture [35], [37]–[39], $\widetilde{R}_{k_{x'},k_{y'}}(\omega)$ is the same as a 3-D Fourier transform of the echo signal over both the transducer aperture and time.

With (1) and (2), images can be reconstructed with the extended HFR imaging methods [35], [37]–[39]. Changing the free parameters, k_{x_T} and k_{y_T}, from one transmission to another, multiple images can be reconstructed (see Section II,C of [35] and Section III of [39] for details of image reconstructions), then combined coherently to form an image of an equivalent dynamic focusing in both transmission and reception of traditional delay-and-sum (D&S) imaging [64] for a stationary object, resulting in an image of both high resolution and contrast over a large field of view. In the following, we will use the same methods as in [35] and [39] for image reconstructions and study the effects of object motions on the extended HFR imaging method. For simplicity, a 2-D version of (1) and (2) (simply setting $k_{y_T} = k_{y_R} \equiv 0$) will be used to reconstruct 2-D images in this paper [35], [37]–[39]. Furthermore, in both computer simulations and *in vitro* experiments, only two conditions, 11 (higher frame rate) and 91 (lower frame rate) transmissions, will be considered. In the *in vivo* experiment, 19

$$\left\{\begin{aligned} R_{k_{x_R}+k_{x_T},k_{y_R}+k_{y_T}}(t) &= \int_V f(\vec{r}_0)\left[\Phi^T_{\text{Array}}(\vec{r}_0,t) * \Phi^R_{\text{Array}}(\vec{r}_0,t)\right] d\vec{r}_0 \\ &= \frac{1}{2\pi}\int\limits_{-\infty}^{\infty} \frac{A(k)T(k)H(k)}{c}\left[\int_V f(\vec{r}_0) e^{i\left(k_{x_R}+k_{x_T}\right)x_0+i\left(k_{y_R}+k_{y_T}\right)y_0+i\left(k_{z_R}+k_{z_T}\right)z_0} d\vec{r}_0\right] e^{-i\omega t} dk \\ &= \frac{1}{2\pi}\int\limits_{-\infty}^{\infty} \frac{A(k)T(k)H(k)}{c} F\left(k_{x_R}+k_{x_T}, k_{y_R}+k_{y_T}, k_{z_R}+k_{z_T}\right) e^{-i\omega t} dk \\ \widetilde{R}_{k'_x,k'_y}(\omega) &= \frac{A(k)T(k)H(k)}{c^2} F\left(k'_x, k'_y, k'_z\right) \end{aligned}\right. , \tag{1}$$

transmissions will also be included. For other numbers of transmissions between these numbers, the degree of motion effects is assumed proportional to the number of transmissions.

III. Computer Simulations

Computer simulations were carried out to study the effects of motions on the extended HFR imaging method under ideal conditions in which there are no noise and other influences of a practical imaging system. In the computer simulations, a 1-D linear array transducer with 128 elements, 0.15-mm pitch (about a quarter of the center wavelength of the array), 14-mm elevation width (without elevation focus), 2.5-MHz center frequency, and 58% −6 dB pulse-echo fractional bandwidth defined by the square of the Blackman window function [6] was assumed. A one-cycle sine wave pulse at the center frequency was used to excite the array. The time between adjacent transmission pulses was 187 μs.

Simulations were performed with both limited-diffraction array beam [29], [30] and steered plane wave [26], [27], [31], [32] transmissions. For limited-diffraction array beam transmissions, the maximum value of k_{x_T} was calculated with $k_{x_T\text{-}\max} = k_c \sin(\pi/4)$, where $k_c = 2\pi f_c/c$, f_c is the center frequency of the array, and $\pi/4$ is a specified maximum equivalent steering angle off the axis of the array at the center frequency. Because for each k_{x_T}, both sine and cosine aperture weightings are needed (see (13) of [35]), 6 and 46 different k_{x_T}, equally spaced from 0 to $k_{x_T\text{-}\max}$, were used to produce 11 and 91 transmissions, respectively. (Because $\sin(0) = 0$, only one transmission was needed for $k_{x_T} = 0$). For steered plane wave transmissions [35]–[39], the steering angles were evenly spaced from $-\pi/4$ to $\pi/4$. The $k_{\min}$ and $k_{\max}$ in (40) and (41) of [39] were set to correspond to 0 and 5 MHz, respectively. In addition, all the spectral components in Figs. 2(b) and 2(d) of [39] are available for image reconstruction. For the conventional D&S method (dynamic reception focusing) with 91 transmissions, the transmission focal depth was set to 70 mm along each transmit direction, and the steering angle, ζ_T, ranged from $-\pi/4$ to $\pi/4$ with an evenly spaced $\sin\zeta_T$ [35]–[39], which means that there were more transmissions at smaller steering angles than at larger ones for the D&S method.

The simulations were done first for a stationary (no motion) point scatterer placed on the axial axis (perpendicular to the surface of the array) at 30, 50, 70, and 90 mm depths. Two-dimensional envelope-detected images (point spread functions or PSFs) were obtained with both the limited-diffraction array beam and steered plane wave transmissions, and the maximum value of each vertical line (in parallel with the axial axis) of the images was plotted versus the lateral axis that was in parallel with the surface of the array (Fig. 1).

From Fig. 1, it is clear that, for all depths, both limited-diffraction array beam and steered plane wave imaging methods with 91 transmissions have better resolution and lower sidelobes than the conventional D&S method of 70-mm transmission focal distance and a dynamically focused reception with the same number of transmissions. At the 30-mm depth, which is far from the focal distance of the D&S imaging, the extended HFR imaging method has much lower sidelobes, even with only 11 transmissions. For the extended HFR imaging method with 91 transmissions, sidelobes increase and image resolution decreases as the depth increases. However, the results are still better than those of the D&S method. It also is noticed that, as the number of transmissions is reduced from 91 to 11, sidelobes are increased and resolution is reduced for the extended HFR imaging method.

To study the effects of motion on the extended HFR imaging methods, the point scatterer in Fig. 1 was allowed to move in either lateral (in parallel with the array) or axial (perpendicular to the surface of the array) direction during the data acquisition. This produces PSFs of moving objects. Results at two depths (30 and 90 mm) are shown in Figs. 2 and 3 with 11 and 91 transmissions, and they are compared to those with a stationary point scatterer. The velocity of the point scatterer is defined as $V = \sqrt{V_x^2 + V_z^2}$, where V_x and V_z are the lateral and axial velocity components, respectively.

In Panels (1) and (2) of Figs. 2 and 3, at the lateral or axial velocity of up to 214 mm/s, the effects of motions on both limited-diffraction array beam and steered plane wave imaging with 11 transmissions are negligible, especially, in a farther distance such as 90 mm. However, as the number of transmissions is increased to 91 [see Panels (3) and (4) in Figs. 2 and 3], both the limited-diffraction array

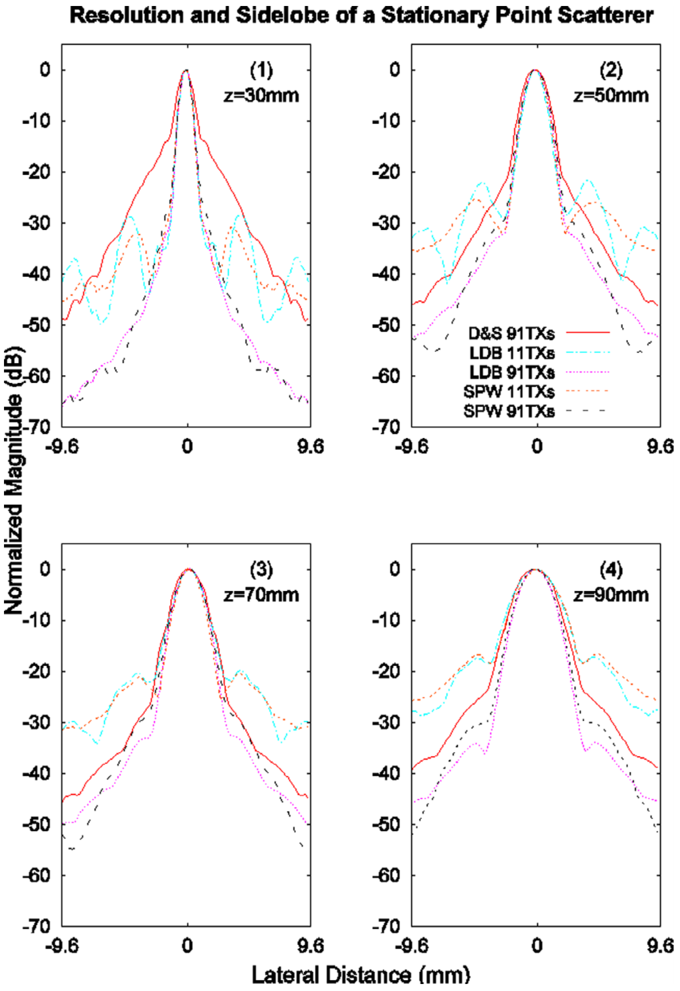

Fig. 1. Sidelobe plots (maxima of envelope-detected images along the axial direction versus the lateral distance that is in parallel with the transducer surface) of computer simulated images of a stationary point scatterer (PSF) located at depths of (1) 30, (2) 50, (3) 70, and (4) 90 mm, respectively, in water. A 2.5 MHz center frequency 1-D array transducer of 128 elements, 0.15 mm pitch, and 58% −6 dB pulse-echo fractional bandwidth was assumed. D&S 91 TXs (red and solid lines): D&S method with 91 transmissions focused at 70 mm and a dynamically focused reception; LDB 11 TXs (cyan and dash-dotted lines) and LDB 91 TXs (pink and dotted lines): limited-diffraction array beam imaging with 11 and 91 transmissions, respectively; SPW 11 TXs (orange and dashed lines) and SPW 91 TXs (black and long-dashed lines): steered plane wave imaging with 11 and 91 transmissions, respectively.

beam and steered plane wave imaging methods are more sensitive to the motions, especially at a distance that is closer to the array. As the velocity increases, the effects of motion are more noticeable. In addition, an axial motion has stronger effects than a lateral one. The motions may significantly reduce the peak value of reconstructed images with elevated sidelobes, especially at a higher velocity.

IV. In Vitro and In Vivo Experiments and Results

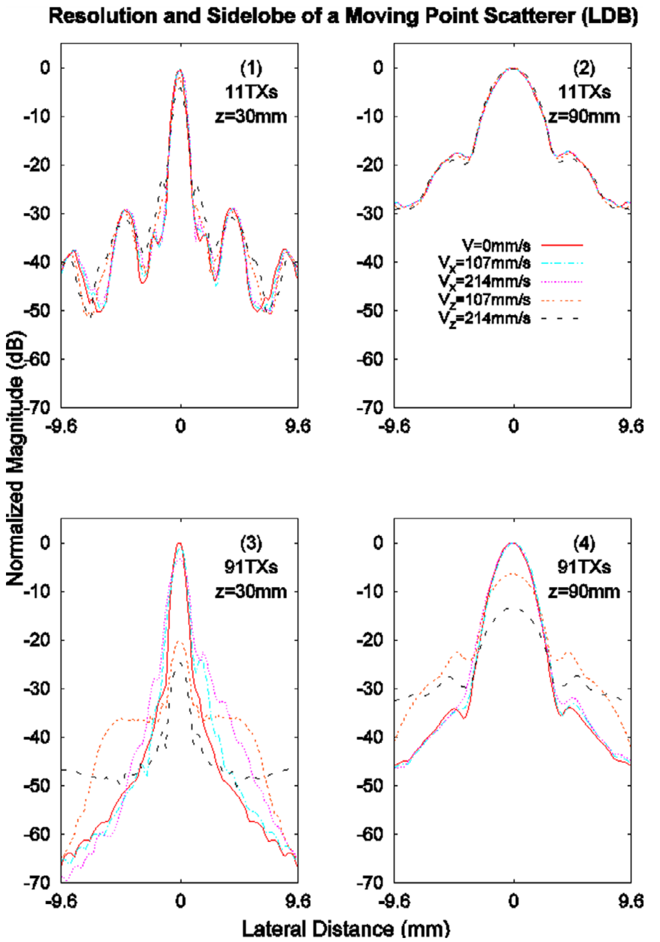

Fig. 2. Sidelobe plots (maxima of envelope-detected images along the axial direction versus the lateral distance that is in parallel with the transducer surface) of computer simulated images of a moving point scatterer (PSF) located at depths of 30 [panels (1) and (3)] and 90 mm [Panels (2) and (4)], respectively, in water. The images were reconstructed with the limited-diffraction array beam imaging method of 11 [panels (1) and (2)] and 91 [panels (3) and (4)] transmissions, respectively. The time between adjacent transmissions was 187 μs. The transducer used was the same as that in Fig. 1. $V = 0$ mm (red and solid lines): the point scatterer was stationary; $V_x = 107$ mm (cyan and dash-dotted lines) and $V_x = 214$ mm (pink and dotted lines): the point scatterer moved at 107 and 214 mm/s along the lateral direction, respectively; $V_z = 107$ mm (orange and dashed lines) and $V_z = 214$ mm (black and long-dashed lines): the point scatterer moved at 107 and 214 mm/s along the axial direction, respectively. The peaks of the plots are relative to the stationary cases.

To study motion effects on the extended HFR imaging method in real conditions, both *in vitro* and *in vivo* experiments were performed using a homemade, general-purpose HFR imaging system [35], [58], [59].

A. Experiment System and Conditions

The imaging system has 128 independent, broadband (0.05–10 MHz), and arbitrary waveform generators (linear power amplifiers) capable of producing up to ± 144 V peak voltage at a 75 Ω resistive load. The accuracy of time delay is 6.25 ns (160 MHz for delay circuits), and the waveforms are produced with a 40-MHz and 12-bit digital-to-analog (D/A) converter in each channel. The system also has

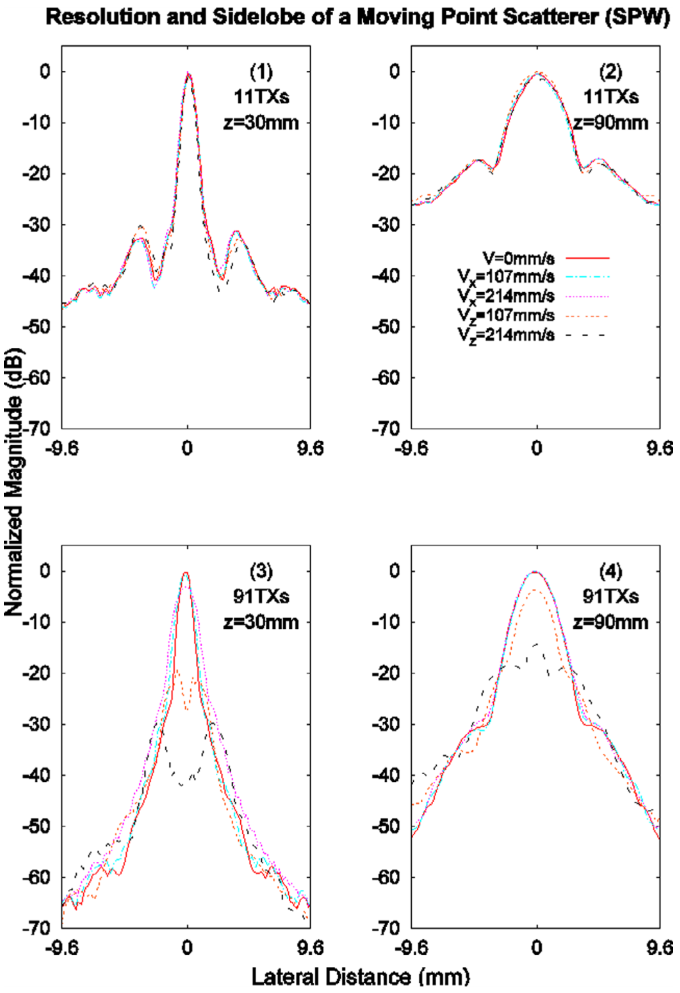

Fig. 3. This figure is the same as Fig. 2, except that steered plane waves, instead of limited-diffraction array beams, were used in transmissions.

128 independent, broadband (0.25–10 MHz), low-noise, and time-gain-control (TGC) amplifiers of up to 108 dB gain. Echo signals in each channel are digitized with a 12-bit analog-to-digital (A/D) converter at 40-MHz sampling rate, then stored in a synchronous, dynamic, random access memory (SDRAM) of up to 512 MB. The system is controlled with a personal computer (PC) via a USB 2.0 port, and data are transferred to the PC with the same port for image reconstructions [35], [58], [59].

An Acuson V2 phased-array transducer (Siemens Medical Solutions USA, Inc., Malvern, PA) was used for both *in vitro* and *in vivo* experiments. The array has the same parameters as those assumed in the simulations, except that it is focused at 68-mm depth in the elevation direction and its −6 dB pulse-echo bandwidth may be smaller.

In the experiments, the same transmission schemes for limited-diffraction array beam, steered plane wave, and D&S imaging methods as those in the simulations were used, except for limited-diffraction array beam transmissions in which cosine and sine functions were replaced with square-wave functions to weight the amplitude of transmitted pulses for different values of k_{x_T} to increase the SNR [35], [36]. The received radio frequency (RF) echo signals were digitized at 40-MHz sampling rate, then down sampled to 10 MHz to reduce computations during image reconstructions for the extended HFR imaging method (for D&S, there was no down sampling because the method is sensitive to the phase accuracy of echo signals) [35]–[39].

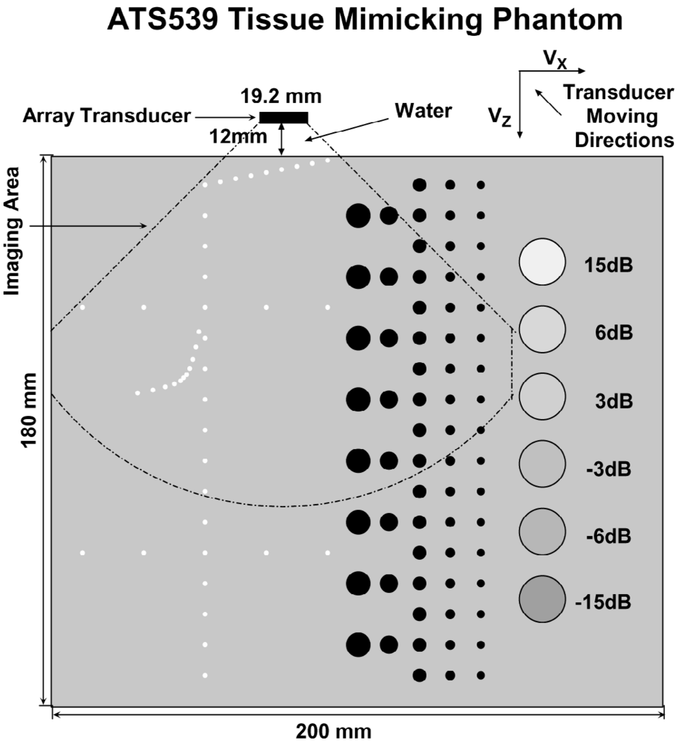

Fig. 4. Structure and imaging area of an ATS539 multipurpose, tissue-mimicking phantom.

B. In Vitro Experiments

In the *in vitro* experiments, an ATS539 multifunction tissue-mimicking phantom was placed on the bottom of a water tank and immersed in water. The phantom was kept stationary during the experiments. The array was clamped to a three-axis scanning system driven by step motors and synchronized with the HFR imaging system. The surface of the array also was immersed in water, and the gap between the array and the phantom was about 12 mm. The structure and imaging area of the ATS539 multipurpose tissue-mimicking phantom are shown in Fig. 4. The phantom has an attenuation of about 0.5 dB/cm/MHz and a speed of sound of about 1450 m/s. The imaging area contains both line and cystic targets. The monofilament nylon line targets have about 0.12-mm diameter each, and the anechoic cylindrical cysts have diameters of 8, 6, 4, 3, 2 mm (from left to right), respectively. Moving directions of the array are indicated in the upper right corner of Fig. 4.

Results of 11 transmissions of limited-diffraction array beam and steered plane wave in different motion conditions are shown in Fig. 5.

The scanning speeds of the array were set to 0 and 214 mm/s in the lateral or axial direction. Images of

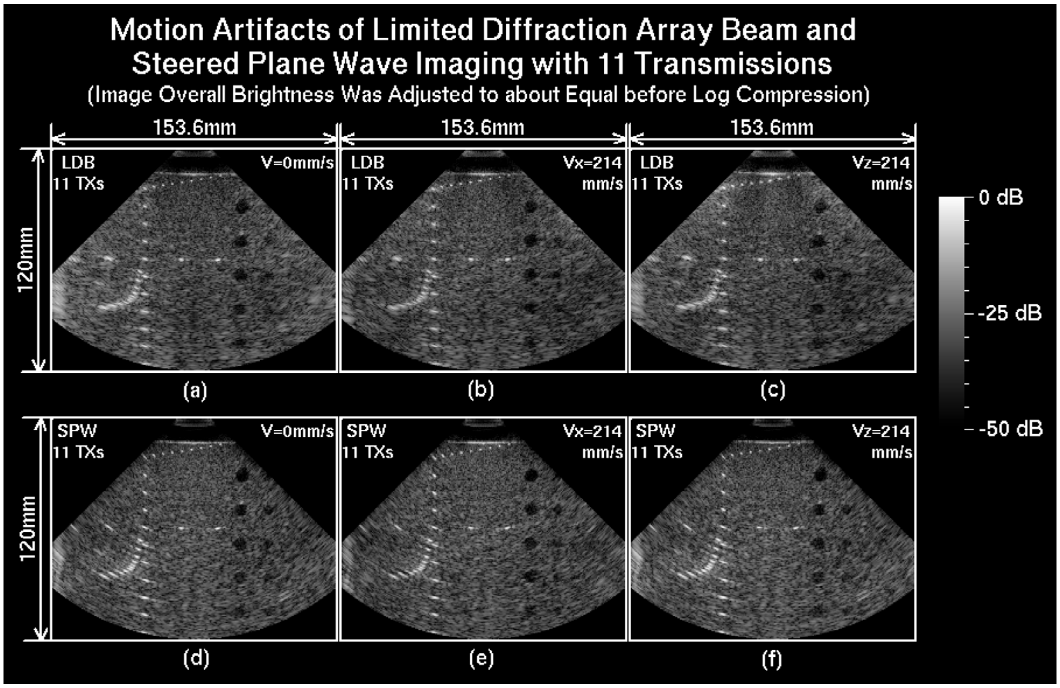

Fig. 5. Images reconstructed with both limited-diffraction array beam and steered plane wave imaging methods with 11 transmissions (TXs) for *in vitro* experiments of an ATS539 tissue-mimicking phantom (see Fig. 4 for the imaging area) immersed in water. The experiments were performed with an Acuson V2 phased array transducer (128 elements, 2.5 MHz, and 0.15-mm pitch) placed near the top of the phantom. The transducer moved at different velocities during data acquisitions, and the phantom was kept stationary. The time between adjacent transmissions was 187 μs. The images are log-compressed with a dynamic range of 50 dB. The speed of sound of the phantom is 1450 m/s, and the depth of images is 120 mm. Results of the limited-diffraction array beam imaging method are shown in (a), (b), and (c) with motion velocities of $V = 0$, $V_x = 214$ mm/s (in the lateral direction), and $V_z = 214$ mm/s (in the vertical direction), respectively. Results of steered plane wave imaging method are shown in (d), (e), and (f), corresponding to (a), (b), and (c), respectively.

limited-diffraction array beam and steered plane wave transmissions are shown in the top and bottom rows, respectively. Results show that there are no obvious motion artifacts for both imaging methods with 11 transmissions, except that there is a slight degradation of image resolution at distances that are very close to the surface of the array at $V_z = 214$ mm for limited-diffraction array beam imaging.

Results for 91 transmissions with limited-diffraction array beams are shown in Fig. 6. The scanning velocities of the array were set to 0, 107, or 214 mm/s in the lateral direction, and 53.5, 107, or 214 mm/s in the axial direction, respectively. The results show that, without motion, both image resolution and contrast are improved significantly as the number of transmissions increases [compare Fig. 6(a) to Fig. 5(a)]. However, motion artifacts are produced if the object is moved during data acquisitions. At a lateral velocity of 107 mm/s [Fig. 5(b)] or axial velocity of 53.5 mm/s [Fig. 5(d)], motion artifacts occur only very near the surface of the array. As the lateral velocity is increased to 214 mm/s [Fig. 5(c)] or the axial velocity is increased to 107 mm/s [Fig. 5(e)], motion artifacts appear in the entire imaging field. It is seen that, at these velocities, the sidelobes of the line targets are increased, and the contrast of the cystic targets is reduced. At an axial velocity of 214 mm/s, severe motion artifacts are observed. Sidelobes for line targets become very large, and the cystic targets are almost buried in the background with nearly zero contrast.

For steered plane waves with 91 transmissions, situations are a little better (Fig. 7). Similar to limited-diffraction array beam imaging, steered plane wave imaging with 91 transmissions produces a higher image quality than 11 transmissions if there is no motion [compare Fig. 7(a) to Fig. 5(d)]. At a lateral velocity of 214 mm/s, only small contrast and sidelobe level changes are observed, except for objects that are very close to the surface of the array. For an axial velocity of 53.5 mm/s, no apparent artifacts are observed. As the axial velocity is increased to 214 mm/s, obvious motion artifacts appear. However, the motion artifacts are less as compared to those of the limited-diffraction array beam imaging under the same conditions.

C. In Vivo Experiments

In vivo experiments were performed on the heart of a healthy volunteer with a procedure approved by the Institute Review Board (IRB) of the University of Toledo. As a comparison, the conventional D&S method also was used to reconstruct images. A transmission pulse sequence was designed to have seven transmission schemes of firing one after another [35]. The transmission sequence is as follows (from the first to the last): steered plane wave with 11, 19, and 91 transmissions, D&S method with 91 transmis-

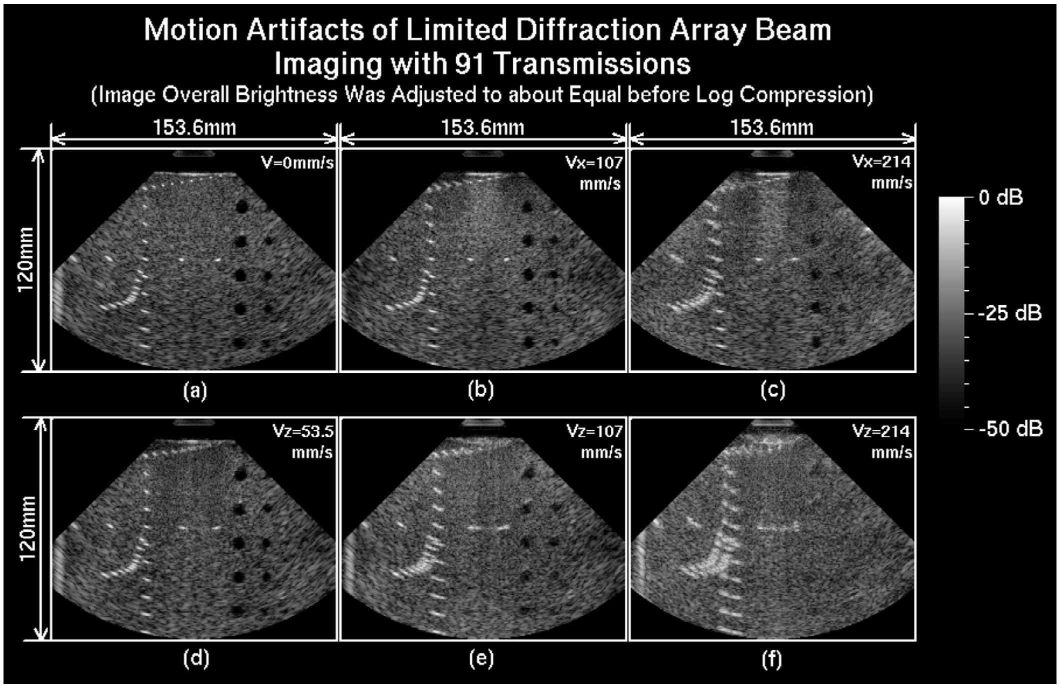

Fig. 6. Images reconstructed with the limited-diffraction array beam imaging method with 91 transmissions (TXs) for *in vitro* experiments of an ATS539 tissue-mimicking phantom (see Fig. 4 for the imaging area) immersed in water. The experimental conditions were the same as those for Fig. 5. Results of different motion velocities ($V = 0$ (stationary), $V_x = 107$ mm/s (in the lateral direction), $V_x = 214$ mm/s, $V_z = 53.5$ mm/s (in the vertical direction), $V_z = 107$ mm/s, and $V_z = 214$ mm/s) are shown in (a)–(f), respectively.

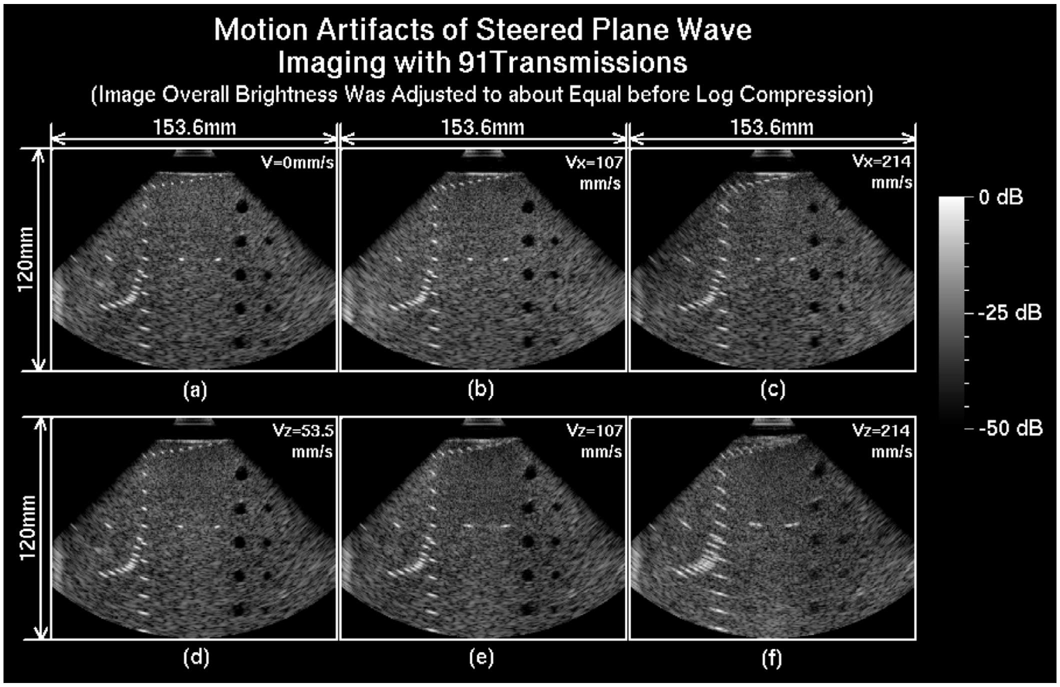

Fig. 7. This figure has the same format and is obtained under the same experimental conditions as those in Fig. 6, except that steered plane waves, instead of limited-diffraction array beams, were used in transmissions.

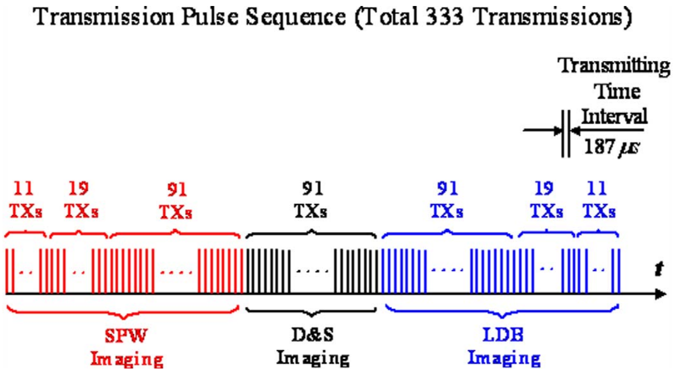

Fig. 8. An illustration of a transmission pulse sequence used for the *in vivo* heart experiment. This sequence was repeated 18 times to cover about one complete heart cycle. SPW, D&S, and LDB mean steered plane wave, delay-and-sum, and limited-diffraction array beam imaging, respectively. 11 TXs, 19 TXs, and 91 TXs represent 11, 19, and 91 transmissions, respectively. The time between adjacent transmissions was 187 μs.

sions, and limited-diffraction array beam with 91, 19, and 11 transmissions (a total 333 transmissions/group). The HFR imaging system was set to have the highest frame rate available for the depth of 120 mm (187 μs between adjacent transmissions). The transmission sequence was repeated 18 times to cover about one heart cycle ($18 \times 333 = 5994$ transmissions, lasting about 1.12 seconds) for a heart rate of 53 beats/minute (see Fig. 14 and the movie of [35] for more details). An illustration of the transmission sequence is shown in Fig. 8.

In the experiment, a commercial Acuson 128XP/10 ultrasound system was used to find a desired cross section of the heart. Once the cross section was found, the array connector was disconnected from the Acuson machine and connected to the HFR imaging system for data acquisition. The data acquisition was triggered by an electrocardiograph (ECG) signal of the volunteer, and 126 images (18×7) were reconstructed. The mitral valve of the heart had the highest peak velocity that was visually measured by tracking the speckles of 18 images of the D&S method. The maximum change of the position of the mitral valve between the neighboring images was found, and the maximum mean velocity was calculated with the following equation:

$$V_{\mathrm{mean\_max}} = \frac{D_{\max}}{T_g}, \tag{5}$$

where $V_{\mathrm{mean\_max}}$ is the maximum mean velocity, $D_{\max}$ is the maximum change of the position of a speckle pattern between neighboring images, and T_g is the time duration for one group of 333 transmissions ($T_g = 333 \times 187$ μs $=$ 62.271 ms). A maximum mean velocity of about 166 mm/s (8.4° relative to the axial axis toward the array) was found on the anterior leaflet of the mitral valve during the rapid ventricular dilatation that pushed the mitral valve open quickly. The vertical bar in the ECG graph of both Figs. 9 and 10 indicates this moment.

Images reconstructed with limited-diffraction array beam and steered plane wave methods near the moment of the peak velocity of the mitral valve are shown in Figs. 9 and 10, respectively. Images obtained with 11, 19, and 91 transmissions have frame rates of about 486, 281, and 59 frames/s, respectively, and are compared well with those of the D&S method with 91 transmissions focused at 70-mm distance with a dynamically focused reception. Compared with the *in vitro* experiments and simulations, no obvious motion artifacts are observed, which may be attributed to the following reasons. First, most places in the imaging field, if they moved, moved at a much lower speed than the peak velocity of the mitral valve. Second, most moving parts in the images (valves, ventricles, and walls) of the heart were near the middle or at farther distances from the array where transmitted beams have fewer overlaps. Third, brighter speckle spots (higher grayscale levels) appear in relatively slow moving parts (such as the heart walls) at farther distances; thus, the motion of the mitral valve does not significantly rescale the entire image. Fourth, although the instantaneous velocity might be high in some places (such as at the leaflets of the mitral valve [65]), the duration of such velocity may be relatively short. Thus it may affect only a small part of transmissions during the data acquisition. (More detailed discussion will be given in Section V.) Due to the reasons above, no apparent motion artifacts have been observed by examining all of the 18 images of each transmission scheme (see [35]). This is different from the simulations or *in vitro* experiments in which an entire object moves at a uniformly high velocity (too extreme from the realistic situations) during the data acquisition leading to severe motion artifacts.

V. DISCUSSION

The extended HFR imaging method with multiple, limited-diffraction array beam or steered plane wave transmissions requires a phase-coherent summation in either spatial or spatial Fourier domain [35]–[39] to increase image resolution. Phase misalignment [66] due to motions during data acquisitions will produce motion artifacts. From both the simulations and experiments, we have found that motion artifacts are related to the following factors.

A. Number of Transmissions

At any given point in an imaging field, the number of coherent superpositions is proportional to the number of overlapping transmissions. As the number of transmissions increases, motion artifacts also increase. With 11 transmissions, overlapping regions are close to the surface of the array transducer. For 91 transmissions, overlapping transmissions appear in the entire imaging area. Thus the superposed image is more sensitive to the motion. In addition, in general, areas that are nearer to the surface of the array are more sensitive to motions than those farther away from the array.

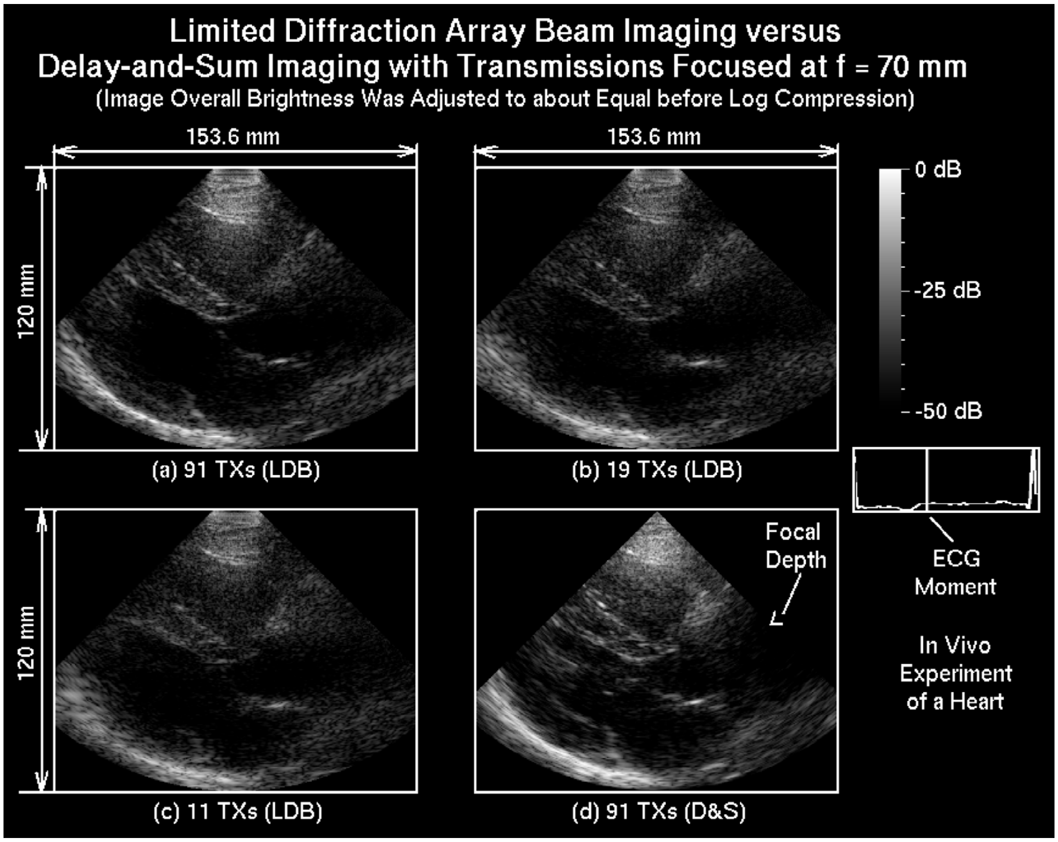

Fig. 9. Images reconstructed from *in vivo* experiments of the heart of a volunteer. The experiment was performed with an Acuson V2 phased-array transducer (128 elements, 2.5 MHz, and 0.15 mm pitch) that was stationary and was in contact with the skin. The time between adjacent transmissions was 187 μs. The images are log-compressed with a dynamic range of 50 dB. The speed of sound was assumed 1540 m/s, and the depth of images was 120 mm. Images in panels (a), (b), and (c) were reconstructed with the limited-diffraction array beam imaging method, with 91, 19, and 11 transmissions, respectively. For comparison, an image reconstructed with the conventional D&S method with a fixed transmission focal distance of 70 mm and a dynamically focused reception was shown in panel (d). The ECG signal in the box below the scale bar indicates the moment when the images were acquired according to the sequence in Fig. 8. (The mitral valve is located at about 20 mm below the center of each subpanel.) (Modified from Fig. 14 of [35] with permission.)

B. Motion Velocity

When the velocity of an object increases, phase misalignment [66] between transmissions increases. Thus more artifacts are produced. Fortunately, most organs of the human body do not move very fast, and fast moving objects such as the leaflets of the heart are confined to a small region. Thus, no severe motion artifacts would appear in these cases (see the *in vivo* experiments of the heart in Figs. 9 and 10).

C. Direction of Motion

Both the simulation and experimental results show that an axial motion produces more artifacts than a lateral one. This is because, for each transmission, spatial frequency in the axial direction is much higher than that in the lateral. Therefore, higher phase coherence is required to avoid motion artifacts in the axial direction. At axial velocities of 53.5, 107, and 214 mm/s, the maximum phase error for 91 transmissions of a limited-diffraction array beam or steered plane wave can be as much as 1.5λ, 3λ, and 6λ, where λ is the wavelength, near the surface of the array, respectively, for a 2.5-MHz array transducer and a speed of sound of 1540 mm/s. However, the same lateral velocities will produce much less phase error. As a result, an axial motion will degrade image quality more quickly than a lateral one.

D. Partial or Entire Imaging Field Motion

Simulation results show that motion may cause the peak intensity of a PSF to drop along with an increase in sidelobe levels. If only a small part of an imaging field is moved, and the mapping of the grayscale of the entire imaging field remains more or less unchanged, motion artifacts may be localized, or a degradation of image quality may appear only in a small region. However, if objects in the entire imaging field are moving, the dynamic range of image may be reduced, resulting in more severe motion artifacts that reduce both image contrast and resolution.

E. Imaging Method

Results also show that limited-diffraction array beam imaging is more sensitive to motion than steered plane wave imaging when the number of transmissions is large (such as 91 transmissions). Further examining the partially reconstructed images from each transmission (in simulations and under the stationary condition), one can see

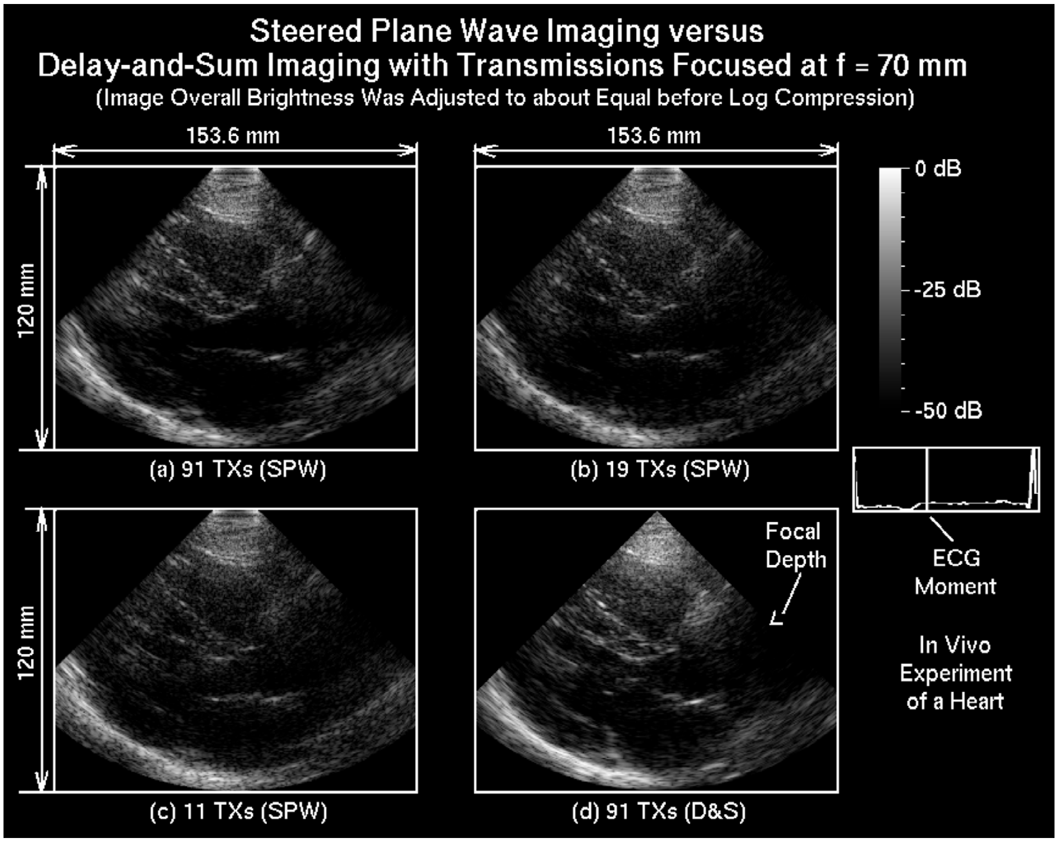

Fig. 10. This figure has the same format and is obtained under the same experimental conditions as those in Fig. 9, except that images in panels (a), (b), and (c) are replaced with the results of the steered plane wave imaging method. (The mitral valve is located at about 20 mm below the center of each subpanel.) (Modified from Fig. 14 of [35] with permission.)

that the two methods form the final PSF differently. For limited-diffraction array beam imaging, sidelobes of the PSF in each partially reconstructed image have different oscillation patterns, and the PSF will not rotate between transmissions. During coherent superposition, the mainlobes of each PSF are added together and sidelobes cancel each other, resulting in a final PSF with much lower sidelobe levels. For steered plane wave imaging, the PSF rotates when plane waves are steered in different directions, which is similar to what Nikolov and Jensen [50] have found for a synthetic transmit aperture ultrasound imaging. During the superposition, sidelobes do not increase and the mainlobe is enhanced coherently, resulting in a similar final PSF as that of limited-diffraction array beam imaging. If objects move between transmissions, sidelobes of the partial PSFs of different limited-diffraction array beam transmissions may not be suppressed effectively, producing more motion artifacts than the steered plane wave imaging. However, if the number of transmissions is small, motion effects on both limited-diffraction array beam and steered plane wave imaging are similar.

F. Effects of Motion on Axial Resolution

It is clear from Figs. 6 and 7 that motions affect mainly lateral resolution, even if the motion is in the axial direction.

G. Possible Ways To Reduce or Compensate Motion Artifacts

Based on the factors discussed above, several approaches can be applied to reduce or compensate for motion artifacts. When imaging fast moving objects, a small number of transmissions can be used for both limited-diffraction array beam and steered plane wave imaging. If fast moving objects are located farther away from the transducer surface, more transmissions can be used to increase image contrast and resolution without significantly increasing the motion artifacts. To reduce motion artifacts, methods similar to those in [53] and [56] could be applied.

VI. CONCLUSIONS

Our previous studies show that the HFR imaging method [26]–[28] can be extended easily to include multiple transmissions of limited-diffraction array beam or steered plane wave to increase both image resolution and field of view, and to reduce sidelobe levels [35]–[39]. In this paper, effects of motion on the extended HFR imaging methods have been investigated [66]. Computer simulations and *in vitro* and *in vivo* experiments were performed, and factors affecting motion artifacts have been discussed. Possible ways to reduce or compensate for motion artifacts are pointed out.

Our studies show that, for both limited-diffraction array beam and steered plane wave imaging, motion artifacts will increase when the number of transmissions or moving velocity increases. Areas near the surface of the transducer are more sensitive to motions than those in farther distances. Lateral motions produce fewer artifacts than axial motions, and motions in a partial imaging field may be less noticeable than those of a whole imaging field. In addition, when a large number of transmissions are used, limited-diffraction array beam imaging is more sensitive to motion than steered plane wave imaging. Fortunately, in most medical imaging applications, organs, structures and tissues keep stationary or move at low speeds during imaging; therefore, both methods are generally good for these applications. However, in extreme conditions, severe artifacts may be produced if a large number of transmissions are used and fast moving objects are located near the transducer surface or in the entire imaging area.

Because the extended HFR methods with multiple, limited-diffraction array beam or steered plane wave transmissions can provide a continuous trade-off between image quality and frame rate, the imaging methods can be optimized according to different clinical applications. When stationary or slowly moving objects are imaged, a lower frame rate (or a larger number of transmissions) can be used to increase image quality. If objects move fast, such as the heart, a higher frame rate (or a smaller number of transmissions) can be used to reduce motion artifacts. This will be more convenient than the conventional D&S method in which the frame rate is less flexible to change given a desired imaging depth and field of view.

Acknowledgment

The authors appreciate Mr. Jiqi Cheng's help in providing part of the image reconstruction programs.

References

[1] J. A. Stratton, *Electromagnetic Theory.* New York: McGraw-Hill, 1941, p. 356.

[2] J. Durnin, "Exact solutions for nondiffracting beams. I. The scalar theory," *J. Opt. Soc. Amer. A*, vol. 4, no. 4, pp. 651–654, 1987.

[3] J. Durnin, J. J. Miceli, Jr., and J. H. Eberly, "Diffraction-free beams," *Phys. Rev. Lett.*, vol. 58, no. 15, pp. 1499–1501, Apr. 13, 1987.

[4] J.-y. Lu and J. F. Greenleaf, "Sidelobe reduction for limited diffraction pulse-echo systems," *IEEE Trans. Ultrason., Ferroelect., Freq. Contr.*, vol. 40, no. 6, pp. 735–746, Nov. 1993.

[5] J.-y. Lu and J. F. Greenleaf, "Theory and acoustic experiments of nondiffracting X waves," in *Proc. IEEE Ultrason. Symp.*, 1991, pp. 1155–1159.

[6] J.-y. Lu and J. F. Greenleaf, "Nondiffracting X waves—Exact solutions to free-space scalar wave equation and their finite aperture realizations," *IEEE Trans. Ultrason., Ferroelect., Freq. Contr.*, vol. 39, no. 1, pp. 19–31, Jan. 1992.

[7] J.-y. Lu and J. F. Greenleaf, "Experimental verification of nondiffracting X waves," *IEEE Trans. Ultrason., Ferroelect., Freq. Contr.*, vol. 39, no. 3, pp. 441–446, May 1992.

[8] J.-y. Lu, H. Zou, and J. F. Greenleaf, "A new approach to obtain limited diffraction beams," *IEEE Trans. Ultrason., Ferroelect., Freq. Contr.*, vol. 42, no. 5, pp. 850–853, Sep. 1995.

[9] J.-y. Lu and A. Liu, "An X wave transform," *IEEE Trans. Ultrason., Ferroelect., Freq. Contr.*, vol. 47, no. 6, pp. 1472–1481, Nov. 2000.

[10] C. Day, "Intense X-shaped pulses of light propagate without spreading in water and other dispersive media," *Physics Today*, vol. 57, no. 10, pp. 25–26, Oct. 2004.

[11] J.-y. Lu, H. Zou, and J. F. Greenleaf, "Biomedical ultrasound beam forming," *Ultrasound Med. Biol.*, vol. 20, no. 5, pp. 403–428, July 1994.

[12] J.-y. Lu and J. F. Greenleaf, "Diffraction-limited beams and their applications for ultrasonic imaging and tissue characterization," in *New Developments in Ultrasonic Transducers and Transducer Systems, Proc. SPIE.* F. L. Lizzi, Ed. vol. 1733, pp. 92–119, 1992.

[13] J.-y. Lu and J. F. Greenleaf, "Ultrasonic nondiffracting transducer for medical imaging," *IEEE Trans. Ultrason., Ferroelect., Freq. Contr.*, vol. 37, no. 5, pp. 438–447, Sep. 1990.

[14] J.-y. Lu and J. F. Greenleaf, "Pulse-echo imaging using a nondiffracting beam transducer," *Ultrasound Med. Biol.*, vol. 17, no. 3, pp. 265–281, May 1991.

[15] J.-y. Lu, T. K. Song, R. R. Kinnick, and J. F. Greenleaf, "In vitro and in vivo real-time imaging with ultrasonic limited diffraction beams," *IEEE Trans. Med. Imag.*, vol. 12, no. 4, pp. 819–829, Dec. 1993.

[16] H. Peng and J.-y. Lu, "High frame rate 2-D and 3-D imaging with a curved or cylindrical array," in *Proc. IEEE Ultrason. Symp.*, 2002, pp. 1725–1728.

[17] J.-y. Lu and J. F. Greenleaf, "Evaluation of a nondiffracting transducer for tissue characterization," in *Proc. IEEE Ultrason. Symp.*, 1990, pp. 795–798.

[18] J.-y. Lu and J. F. Greenleaf, "Producing deep depth of field and depth-independent resolution in NDE with limited diffraction beams," *Ultrason. Imag.*, vol. 15, no. 2, pp. 134–149, Apr. 1993.

[19] J.-y. Lu, X.-L. Xu, H. Zou, and J. F. Greenleaf, "Application of Bessel beam for Doppler velocity estimation," *IEEE Trans. Ultrason., Ferroelect., Freq. Contr.*, vol. 42, no. 4, pp. 649–662, July 1995.

[20] J.-y. Lu, Z. Wang, and S.-J. Kwon, "Blood flow velocity vector imaging with high frame rate imaging methods," in *Proc. IEEE Ultrason. Symp.*, vol. 2, 2006, pp. 963–966.

[21] J.-y. Lu and J. Cheng, "Field computation for two-dimensional array transducers with limited diffraction array beams," *Ultrason. Imag.*, vol. 27, no. 4, pp. 237–255, Oct. 2005.

[22] J.-y. Lu and S. He, "Optical X waves communications," *Opt. Commun.*, vol. 161, pp. 187–192, Mar. 1999.

[23] J.-y. Lu, J. Cheng, and B. Cameron, "Low sidelobe limited diffraction optical coherence tomography," in *Coherence Domain Optical Methods in Biomedical Science and Clinical Applications VI, Proc. SPIE.* V. V. Tuchin, Ed. vol. 4619, pp. 300–311, 2002.

[24] P. Di Trapani, G. Valiulis, A. Piskarskas, O. Jedrkiewicz, J. Trull, C. Conti, and S. Trillo, "Spontaneously generated X-shaped light bullets," *Phys. Rev. Lett.*, vol. 91, art. no. 093904, 2003.

[25] C. Conti and S. Trillo, "Nonspreading wave packets in three dimensions formed by an ultracold Bose gas in an optical lattice," *Phys. Rev. Lett.*, vol. 92, art. no. 120404, 2004.

[26] J.-y. Lu, "2-D and 3-D high frame rate imaging with limited diffraction beams," *IEEE Trans. Ultrason., Ferroelect., Freq. Contr.*, vol. 44, no. 4, pp. 839–856, July 1997.

[27] J.-y. Lu, "Experimental study of high frame rate imaging with limited diffraction beams," *IEEE Trans. Ultrason., Ferroelect., Freq. Contr.*, vol. 45, no. 1, pp. 84–97, Jan. 1998.

[28] J.-y. Lu, "Transmit-receive dynamic focusing with limited diffraction beams," in *Proc. IEEE Ultrason. Symp.*, 1997, pp. 1543–1546.

[29] J.-y. Lu, "Limited diffraction array beams," *Int. J. Imaging Syst. Technol.*, vol. 8, no. 1, pp. 126–136, Jan. 1997.

[30] J.-y. Lu, "Improving accuracy of transverse velocity measurement with a new limited diffraction beam," in *Proc. IEEE Ultrason. Symp.*, 1996, pp. 1255–1260.

[31] J.-y. Lu and S. He, "Increasing field of view of high frame rate ultrasonic imaging," *J. Acoust. Soc. Amer.*, vol. 107, no. 5, pt. 2, p. 2779, May 2000 (abs).

[32] J.-y. Lu, "Nonlinear processing for high frame rate imaging," *J. Ultrasound Medicine*, vol. 18, no. 3 (Suppl.), p. S50, Mar. 1999 (abs).

[33] G. Wade, "Human uses of ultrasound: Ancient and modern," *Ultrasonics*, vol. 38, pp. 1–5, 2000.

[34] P. N. T. Wells, "Ultrasound imaging," *Phys. Med. Biol.*, vol. 51, no. 13, pp. R83–R98, 2006.

[35] J.-y. Lu, J. Cheng, and J. Wang, "High frame rate imaging system for limited diffraction array beam imaging with square-wave aperture weightings," *IEEE Trans. Ultrason., Ferroelect., Freq. Contr.*, vol. 53, no. 10, pp. 1796–1812, Oct. 2006.

[36] J.-y. Lu and J. Wang, "Square-wave aperture weightings for reception beam forming in high frame rate imaging," in *Proc. IEEE Ultrason. Symp.*, vol. 1, 2006, pp. 124–127.

[37] J.-y. Lu and J. Cheng, "System for extended high frame rate imaging with limited diffraction beams," United States Patent, (Filed) PCT, WO 2007/027703 A3.

[38] J. Cheng and J.-y. Lu, "Fourier based imaging method with steered plane waves and limited-diffraction array beams," in *Proc. IEEE Ultrason. Symp.*, 2005, pp. 1976–1979.

[39] J. Cheng and J.-y. Lu, "Extended high frame rate imaging method with limited diffraction beams," *IEEE Trans. Ultrason., Ferroelect., Freq. Contr.*, vol. 53, no. 5, pp. 880–899, May 2006.

[40] J. Wang and J.-y. Lu, "A study of motion artifacts of Fourier-based image construction," in *Proc. IEEE Ultrason. Symp.*, 2005, pp. 1439–1442.

[41] M. Soumekh, "Array imaging with beam-steered data," *IEEE Trans. Image Processing*, vol. 1, no. 3, pp. 379–390, July 1992.

[42] T. R. Nelson, D. H. Pretorius, A. Hull, M. Riccabona, M. S. Sklansky, and G. James, "Source and impact of artifacts on clinical three-dimensional ultrasound imaging," *Ultrasound Obstet. Gynec.*, vol. 16, no. 4, pp. 374–383, 2000.

[43] R. L. Maurice and M. Bertrand, "Speckle-motion artifacts under tissue shearing," *IEEE Trans. Ultrason., Ferroelect., Freq. Contr.*, vol. 46, no. 3, pp. 584–594, May 1999.

[44] C.-C. Shen and P.-C. Li, "Motion artifacts of pulse inversion-based tissue harmonic imaging," *IEEE Trans. Ultrason., Ferroelect., Freq. Contr.*, vol. 49, no. 9, pp. 1203–1211, Sep. 2000.

[45] F. Kallel, M. Bertrand, and J. Meunier, "Speckle motion artifacts under tissue rotation," *IEEE Trans. Ultrason., Ferroelect., Freq. Contr.*, vol. 41, no. 1, pp. 105–122, Jan. 1994.

[46] F. Kallel and J. Ophir, "Three-dimensional tissue motion and its effect on image noise in elastography," *IEEE Trans. Ultrason., Ferroelect., Freq. Contr.*, vol. 44, no. 6, pp. 1286–1296, Nov. 1997.

[47] L. S. Taylor, D. J. Rubens, and K. J. Parker, "Artifacts and artifact reduction in sonoelastography," in *Proc. IEEE Ultrason. Symp.*, vol. 2, 2000, pp. 1849–1852.

[48] Y. Shi, F. J. de Ana, S. J. Chetcuti, and M. O'Donnell, "Motion artifact reduction for IVUS-based thermal strain Imaging," *IEEE Trans. Ultrason., Ferroelect., Freq. Contr.*, vol. 52, no. 8, pp. 1312–1319, Aug. 2005.

[49] H. Wang, E. S. Ebbini, M. O'Donnell, and C. A. Cain, "Phase aberration correction and motion compensation for ultrasonic hyperthermia phased arrays: Experimental results," *IEEE Trans. Ultrason., Ferroelect., Freq. Contr.*, vol. 41, no. 1, pp. 34–42, Jan. 1994.

[50] S. I. Nikolov and J. A. Jensen, "K-space model of motion artifacts synthetic transmit aperture ultrasound imaging," in *Proc. IEEE Ultrason. Symp.*, 2003, pp. 1569–1573.

[51] S. I. Nikolov and J. A. Jensen, "Velocity estimation using synthetic aperture imaging," in *Proc. IEEE Ultrason. Symp.*, 2001, pp. 1409–1412.

[52] L. F. Nock and G. E. Trahey, "Synthetic aperture imaging in medical ultrasound with correction for motion artifacts," in *Proc. IEEE Ultrason. Symp.*, 1990, pp. 1597–1603.

[53] J.-S. Jeong, J.-S. Hwang, M.-H. Bae, and T.-K. Song, "Effects and limitations of motion compensation in synthetic aperture techniques," in *Proc. IEEE Ultrason. Symp.*, vol. 2, 2000, pp. 1759–1762.

[54] K. S. Kim, J. S. Hwang, J. S. Jeong, and T. K. Song, "An efficient motion estimation and compensation method for ultrasound synthetic aperture imaging," *Ultrason. Imag.*, vol. 24, no. 2, pp. 81–99, Apr. 2002.

[55] M. Karaman, H. S. Bilge, and M. O'Donnell, "Adaptive multi-element synthetic aperture imaging with motion and phase aberation correction," *IEEE Trans. Ultrason., Ferroelect., Freq. Contr.*, vol. 42, pp. 1077–1087, 1998.

[56] K. L. Gammelmark and J. A. Jensen, "Duplex synthetic aperture imaging with tissue motion compensation," in *Proc. IEEE Ultrason. Symp.*, 2003, pp. 1569–1573.

[57] C. R. Hazard and G. R. Lockwood, "Effects of motion on a synthetic aperture beamformer for real-time 3-D ultrasound," in *Proc. IEEE Ultrason. Symp.*, 1999, pp. 1221–1224.

[58] J.-y. Lu and J. L. Waugaman, "Development of a linear power amplifier for high frame rate imaging system," in *Proc. IEEE Ultrason. Symp.*, 2004, pp. 1413–1416.

[59] J.-y. Lu, "A multimedia example," *IEEE Trans. Ultrason., Ferroelect., Freq. Contr.*, vol. 50, no. 9, p. 1078, Sep. 2003.

[60] A. C. Kak and M. Slaney, *Principle of Computerized Tomographic Imaging.* New York: IEEE Press, 1987, ch. 6.

[61] M. Born and E. Wolf, *Principles of Optics.* 7th ed. Cambridge: Cambridge Univ. Press, 1999, ch. 13.

[62] C. S. Kino, *Acoustic Waves: Devices, Imaging and Analog Signal Processing.* Englewood Cliffs, NJ: Prentice-Hall, 1987.

[63] R. Bracewell, *The Fourier Transform and Its Applications.* New York: McGraw-Hill, 1965, ch. 4 and 6.

[64] B. D. Steinberg, "Digital beamforming in ultrasound," *IEEE Trans. Ultrason., Ferroelect., Freq. Contr.*, vol. 39, no. 6, pp. 716–721, Nov. 1992.

[65] M. T. Upton, D. G. Gibson, and D. J. Brown, "Instantaneous mitral value leaflet velocity and its relation to left ventricular wall movement in normal subjects," *Br. Heart J.*, vol. 38, pp. 51–58, 1976.

[66] J. Wang and J.-y. Lu, "Effects of phase aberration and noise on extended high frame rate imaging," *Ultrason. Imag.*, vol. 29, no. 2, Apr. 2007.

Jing Wang was born in Beijing, China, in 1973. He received the B.S. degree and the M.S. degree in analytical instrument engineering and precision instrument engineering in 1996 and 2000, respectively, both from Tianjin University, Tianjin, China. He is currently pursing his doctorate degree in the Department of Bioengineering at the University of Toledo, Toledo, OH.

His research interests in ultrasound include new imaging technique development and implementation, imaging process optimization, motion artifacts, and phase aberration corrections.

Jian-yu Lu (S'86–M'88–SM'99) received the B.S. degree in electrical engineering in February 1982 from Fudan University, Shanghai, China; the M.S. degree in acoustics in 1985 from Tongji University, Shanghai, China; and the Ph.D. degree in biomedical engineering in 1988 from Southeast University, Nanjing, China.

From 1997 to the present, Dr. Lu has been a professor in the Department of Bioengineering and an adjunct professor in the College of Medicine at the University of Toledo, Toledo, OH. He served as a graduate director of the Department of Bioengineering at the University of Toledo from 1999–2002. Before joining the University of Toledo, he was an associate professor of biophysics at the Mayo Medical School and an associate consultant at the Department of Physiology and Biophysics, Mayo Clinic/Foundation, Rochester, MN. His research interests are in acoustic imaging and tissue identification, medical ultrasonic transducers, and ultrasonic beam forming and propagation.

Dr. Lu received the Outstanding Paper Award from the UFFC society for two of his papers published in the *IEEE Transactions on Ultrasonics, Ferroelectrics, and Frequency Control* in 1992 for the discovery of X waves that, in theory, can propagate to an infinite distance without spreading (diffraction-free). These waves have potential applications in medical imaging (in both ultrasound and optics) and physics. He received the Edward C. Kendall (a Nobel Laureate at Mayo Clinic) Award from the Mayo Alumni Association, Mayo Foundation, in 1992, for his meritorious research; the FIRST Award from the National Institutes of Health (NIH) in 1991; and the Biomedical Engineering Research Grant Award from the Whitaker Foundation in 1991, in addition to other long-term, R01-type NIH grant awards.

He has been the Editor-in-Chief of the *IEEE Transactions on Ultrasonics, Ferroelectrics, and Frequency Control* since January 2002. He is a general co-chair of the 2008 IEEE International Ultrasonics Symposium (IEEE IUS) that will be held in Beijing, China. In addition, he served as the Technical Program Chair of the 2001 IEEE IUS—a joint meeting with the World Congress on Ultrasonics (WCU) held in Atlanta, GA, in October 2001. He has been a member of Group I (Medical Ultrasonics) of the Technical Program Committee of the IEEE IUS since 2000. He also serves on both the UFFC Ultrasonics Committee and the UFFC Web Committee. He was an exhibition chair of the IEEE IUS for many years. Dr. Lu is a Fellow of the American Institute of Ultrasound in Medicine (AIUM), a Fellow of the American Institute for Medical and Biological Engineering (AIMBE), and a senior member of the IEEE UFFC Society, in addition to being a member of other professional societies such as the Acoustical Society of America (ASA), American Association for the Advancement of Science (AAAS), and Sigma Xi.